Surface Roughness Effects On Cavity Flows

Ganesh Nampelly[1], Ananth Sivaramakrishna Malathi[1], Aditya Vaid[1], Nagabhushana Rao Vadlamani[1*], Sriram Rengarajan[1] and Konstantinos Kontis[2]

[1]Department of Aerospace Engineering, Indian Institute of Technology, Madras, Chennai, 600036, Tamilnadu, India.
[2]Division of Aerospace Sciences, University of Glasgow, Glasgow, G128QQ, United Kingdom.

*Corresponding author(s). E-mail(s): nrv@iitm.ac.in;

Abstract

Effects of three-dimensional (3-D) distributed roughness elements on the flow characteristics within a cavity are investigated using a series of high-fidelity eddy-resolving simulations. The cavity flows generate undesirable low-frequency pressure fluctuations due to the vortex impingement over the trailing edge of the cavity. We explore the possibility of employing distributed hemispherical roughness elements as a passive flow control strategy towards suppressing these pressure fluctuations. A rectangular cavity with a length to depth ratio, $\boldsymbol{L/D}$, of 3 is considered. Simulations are carried out at a Mach number of 0.2 and Reynolds numbers of 7000 and 19300, based on the free-stream velocity and the depth of the cavity. The effect of sparsely and densely packed roughness elements on the stability of shear layer separating from the cavity are brought out. Pre-transitional fluctuations generated by the roughness elements (a) resulted in transitional/turbulent flow at the cavity leading edge for low/high Reynolds numbers (b) promoted an earlier breakdown of the large-scale coherent structures in the shear layer (c) decreased the 'cavity tones' and the associated sound pressure levels (SPL) by 5-13 dB. Reduction in SPL is observed to be prominent at higher Reynolds numbers and with dense spacing between the roughness elements. At low Reynolds numbers, the benefit obtained by suppressing the 'cavity tones' can be eclipsed with an increase in the broadband noise.

Keywords: Cavity, Roughness, Rossiter, Sound Pressure Level, Shear Layer

1 Introduction

Cavity flows are encountered in a wide range of engineering applications which include but not limited to aeroacoustics [1, 2] measurement windows of airplane configurations [3], automotive vehicle door gaps [4], flow induced vibrations [5] and gravel-bed rivers in hydraulic systems [6]. It has hence been a major topic of interest within the research community for several decades, and numerous experimental and computational investigations have been carried out in this front [1, 7]. Flows within the cavities are highly unsteady, particularly at high Reynolds numbers. They are characterized by destabilizing separated shear layers, unsteady interaction of vortices of different scales within the cavity, strong reverse flows, etc. Typically, the boundary layer developing upstream of the cavity separates at the cavity leading edge. The separated shear layer is prone to Kelvin-Helhmotz (KH) instabilities which are amplified in the streamwise direction. This leads to the roll-up of the shear layer and subsequent formation of vortices. At higher Reynolds numbers, these vortices further breakdown into smaller scales enhancing turbulence. The impingement of these vortices on the trailing edge of the cavity walls causes intense pressure perturbations. When the frequency of these acoustic waves coincides with the frequency of the shedding of the shear layer, resonance can occur. This is referred to as shear layer or Rossiter mode instability [8]. The self-sustaining oscillations due to the Rossiter instability is influenced by numerous parameters such as length and depth of the cavity, Mach number, and the fluid dynamic properties of the incoming boundary layer [9, 10].

Sun et al. [11] investigated the effects of Mach number on the cavity flows. Increasing the Mach number destabilized the shear layer in the subsonic regime ($0.1 < M < 0.8$)), while it stabilizes in the transonic regime ($0.8 < M < 1.6$). Ganesh et al. [12] analyzed the effect of Reynolds number on the shear layer instability in an open cavity of $L/D = 3$ at different Reynolds numbers. As expected, higher Reynolds number resulted in an early destabilization of the shear layer and a stronger recirculation zone within the cavity. In addition to the Rossiter instability, flow within cavities also experience centrifugal instability which is three-dimensional and occurs within the recirculation zone [7, 13]. Cavities exhibit another mode of instability known as wake mode, as the cavity length increases in comparison to the incoming boundary layer thickness. It is distinguished by the periodic expulsion of the large-scale vortices from the cavity [14].

Unsteady flow interactions within the cavity degrades the aerodynamic performance and increases the structural loading. For example, these unsteady interactions are shown to cause thermo-acoustic instabilities in the scramjet combustor [15]. Several passive or active flow control strategies have been proposed in the literature to suppress such undesirable oscillations in the cavity. The shear layer developing from the leading edge of the cavity becomes unsteady due to the pressure difference between the free-stream and cavity. Heller and Bliss [16] demonstrated an appreciable reduction in the pressure levels by slanting the cavity's trailing edge. It ensures that the shear layer

remained uncurved over the cavity length, thereby achieving a steady stagnation point and a proper impingement angle at the rear bulk head. Baysal et al. [17] investigated the effects of trailing edge ramp and leading edge spoiler on the cavity flow oscillations. The solid ramp was found to suppress the acoustics by altering the wave pattern and pressure distribution within the cavity. The vertical spoiler deflected the shear layer upward, thereby modifying the vortex shedding pattern and pressure distribution. Compared to the ramp, the spoiler was found to be more effective in suppressing the peak pressure. Vakili et al. [18] on the other hand used active flow control by injecting high momentum fluid upstream of the cavity using an external pressurized tank and observed a 27dB reduction in the peak pressure.

In most of these studies, the surfaces of the cavity are assumed to be aerodynamically smooth while in reality, the surfaces can gradually roughen with time. For example, the agglomeration of the unburnt fuel or spallation of surfaces at high temperatures in the combustion chamber can roughen the cavity walls and subsequently alter the flow behaviour. To the authors' knowledge, limited studies in the literature have addressed the effects of surface roughness on cavity flows. Wang et al. [19] investigated the behaviour of cavity oscillations employing a dimpled surface upstream of a deep cavity with $L/D = 0.3$, where D is depth of the cavity. The dimpled surface promoted transition thereby turning the boundary layer turbulent upstream of the cavity leading edge. This had an effect in reducing the sound intensity levels. Ganesh et al. [20] investigated the effect of hemispherical surface roughness elements on cavity flows. It has been observed that, for a given Reynolds number, the presence of roughness elements promoted earlier transition of the shear layer, thus reducing the maximum sound pressure level by $\approx$ 7dB.

In this paper, we explore the possibility of employing distributed hemispherical roughness elements, which protrude into the boundary layer, towards suppressing the pressure fluctuations in open cavities. We report the results from a series of high-fidelity eddy resolving simulations on a rectangular cavity with a high aspect ratio, $L/D = 3$. In contrast to our earlier study [20], we report the results on two different roughness distributions (sparse/densely packed elements) at two different Reynolds numbers and draw comparisons against the smooth cavity case. The effect of surface roughness distribution on the Rossiter modes, shear layer and centrifugal instabilities in cavities are also brought out.

The paper is organised as follows: Section 2 describes the computational domain with boundary conditions in addition to the test cases and numerical framework considered for the current study. Section 3.1 presents the grid sensitivity study and the validation of the current framework against the experiments. The dynamics of the boundary layer developing upstream of the cavity leading edge are investigated in detail in Section 3.2. In Section 3.3, the shear layer/centrifugal instabilities within the cavity are examined and the efficacy of roughness elements towards reducing the sound pressure level in cavities is demonstrated. Finally, concluding remarks are provided in Section 4.

2 Computational setup

2.1 Computational Domain and Boundary Conditions

The dimensions of the baseline cavity considered in this study is inline with the low-speed experiments conducted at the University of Glasgow [21]. The close circuit tunnel's length, width, and height are 4m, 2.7m, and 2.1m, respectively [22]. Figure 1 shows the schematic of the computational setup as well as the boundary conditions imposed. The distance between the elliptic leading edge to the leading edge of the cavity, L, is chosen as a characteristic length to non-dimensionalize all length scales, while all the velocities are non-dimensionsalized using the free-stream velocity, U_0.

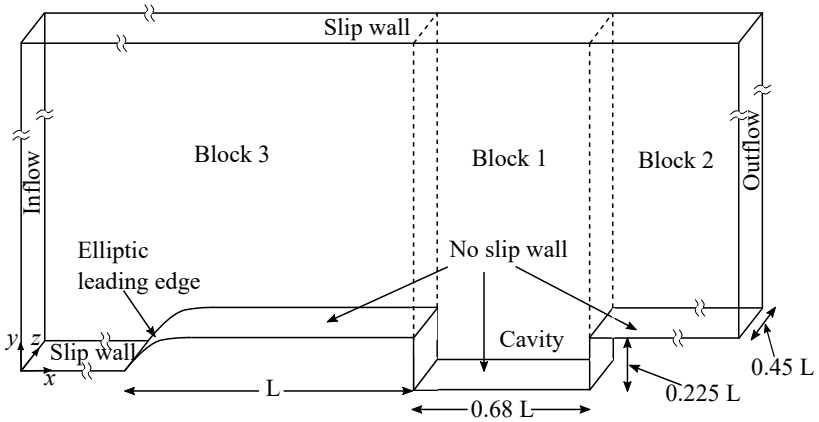

Fig. 1 Schematic of the computational domain with boundary conditions

The overall computational domain has a size of $Lx \times Ly \times Lz = 13L \times 5L \times 0.45L$ ($58D \times 20D \times 2D$) in the streamwise, wall-normal and spanwise directions. A slip wall boundary condition is imposed on the entire top boundary and on the bottom wall from inlet to the elliptic leading edge at $x/L = 5$. On these slip walls, the velocity component normal to the boundary is set to zero [23]. A no-slip condition is imposed beyond $x/L = 5$ on the bottom wall which include all the cavity walls. Following Rizzetta and Visbal [24, 25], fourth-order accurate zero normal pressure gradient has been imposed on the no-slip walls which are maintained at a non-dimensional isothermal temperature of $T = 1.008$ (which corresponds to the adiabatic wall temperature). Periodic conditions are imposed in the spanwise direction. A non-reflective boundary condition based on Riemann invariants is imposed at the inflow as described in Matsuura and Kato [26]. The total pressure and total temperature are held at uniform values of 101.3 kPa and 294.4 K while the outlet static pressure is set to 98.5 kPa. For all the simulations reported in this paper, the inflow is uniform and we have not used any synthetic eddy methods to impose free-stream turbulence at the inlet. Following the approach of Rizzetta and Visbal [24, 27],

any spurious reflections from the outlet and top boundaries are avoided by stretching the mesh beyond $x/L > 8.5$ and $y/L > 0.4$ respectively.

2.2 Numerical Framework

Eddy-resolving simulations of three-dimensional Navier-Stokes equations are carried out using an in-house structured compressible solver COMP-SQUARE. The solver has been largely developed on the basis of the numerical algorithms described in [25, 28]. The continuity, momentum and energy equations are solved in non-dimensional conservative form to predict the conservative variables $(\rho, \rho u, \rho v, \rho w, \rho E)$ and the standard perfect gas law $(P = \rho RT)$ is used to close the set of governing equations. Here, ρ, P, T, E, R represent the density, pressure, temperature, total energy and gas constant respectively, while u, v, w are the cartesian components of the velocity. The details of the governing equations in the generalized (curvilinear) coordinates and the high order numerical schemes to solve these coupled equations in conservative form are discussed in [25, 28, 29]. The solver is equipped with high order explicit and compact finite difference schemes ranging from 2^{nd} to 6^{th} order spatial accuracy. An implicit filter of up to 10^{th} order accuracy with a variable filter coefficient $(-0.5 < \alpha_f < 0.5)$ is used to eliminate any spurious oscillations resulting from the non-dissipative nature of the central difference schemes. Visbal and Gaitonde [30] demonstrate the superior performance of the implicit filter over their explicit counterparts or sub-grid scale (SGS) models in the context of capturing inviscid shear-layer instabilities and viscous boundary layers on stretched grids for low-Mach number flows. Hence, following their strategy, all the simulations reported in this paper are performed using implicit filters without resorting to any SGS models. The solver is parallelized to scale on multi-GPUs and CPUs using OpenACC and MPI strategies, respectively. COMPSQUARE has been validated on several canonical test cases (like Taylor green vortex, inviscid vortex convection, turbulent channel flows/boundary layers [29, 31, 32]) and test cases of industrial relevance (crosswind flows over intakes, separation induced transition on airfoils, etc [33–35]). The explicit schemes are around 2× faster than the compact schemes albeit at a marginal reduction in the accuracy. Hence, of the spatial discretizations schemes available in the solver, we have used the explicit 4^{th} order finite difference scheme to estimate the spatial derivatives both in the interior domain and at the boundaries (using one-sided stencils of the same order). An implicit filter of 6^{th} order with $\alpha_f = 0.48$ is used to maintain the stability and accuracy of the schemes. An explicit four stage 4^{th} order Runge Kutta scheme is used to integrate the solution in time.

Table 1 summarizes the details of test cases investigated in this study along with the corresponding acronyms. Two different Reynolds numbers, Re_L, are considered: 31250 for LRC-Low Reynolds Case and 86000 for HRC-High Reynolds Case. Here, Re_L is defined based on the characteristic length, L, and free-stream velocity, U_0. In terms of the cavity depth, D, and U_0, the Reynolds numbers for LRC and HRC are 7000 and 19300 respectively. Figure

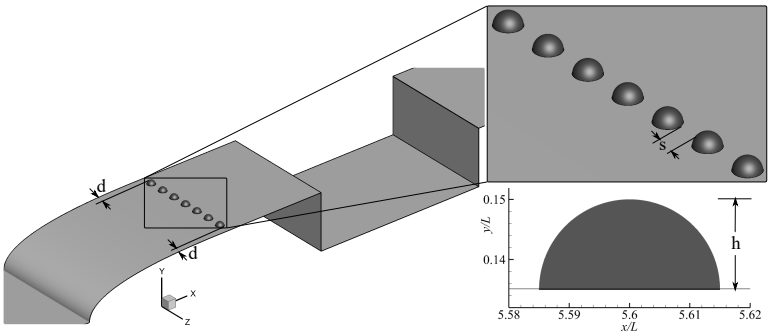

Fig. 2 Schematic of hemispherical roughness elements distribution

2 shows the schematic of hemispherical roughness elements distributed along the span. An inset plot shows the dimensions of the roughness elements which are positioned at x/L=5.6 from the inlet. This corresponds to a location of $x/L = 0.6$ downstream of the elliptic leading edge of the flat plate and $x/L = 0.4$ upstream of the cavity leading edge. Table 2 lists the height (h) and diameter (d) of the roughness elements. Of the two roughness distributions (A & B) considered, the roughness elements are sparsely spaced in A ($s/L = 0.03$) and densely spaced in B ($s/L = 0.015$). The roughness height, h, is chosen to be $3\delta/4$, where δ is the local boundary layer thickness estimated for the smooth cavity LRC case at x/L=5.6. The roughness height is held constant for all the test cases reported. Hence, at high Reynolds number (HRC), the $h/\delta \approx 1.17$ and roughness element penetrates through the boundary layer. Second order Boundary data immersion method (BDIM) [36] is employed to represent the hemispherical roughness elements. In this technique, the boundary conditions on the roughness surface are imposed through a meta equation which maps the compressible Navier-stokes equations in the fluid domain with the governing equation of the solid body, across a fluid-solid interface of finite width of 2ϵ, where ϵ is the kernel radius. This finite region ensures a smooth transition of flow parameters and also avoids the necessity to treat freshly cleared grid points, while performing moving body simulations. For a generic field variable Φ_ϵ, the BDIM meta equation is given as follows:

$$\Phi_\epsilon = f(\Phi, \vec{x}, t)\mu_0^{\epsilon,F} + b(\Phi, \vec{x}, t)(1 - \mu_0^{\epsilon,F}) + \mu_1^{\epsilon,F}\frac{\partial}{\partial n}(f(\Phi, \vec{x}, t) - b(\Phi, \vec{x}, t)) \quad (1)$$

Here $f(\Phi, \vec{x}, t)$ and $b(\Phi, \vec{x}, t)$ denote the field variable values in the fluid and body regions, respectively. $\mu_0^{\epsilon,F}$ and $\mu_1^{\epsilon,F}$ are the zeroth and first moments of the Kernel function, respectively. These moments act as the interpolating functions connecting the solid and fluid sub domains. $\mu_0^{\epsilon,F}$ is unity in the fluid domain, zero in the solid domain and transitions smoothly between 0 and 1 across the solid-fluid interface. The term involving the derivative in the direction normal to the solid body is the correction term that provides second order

accuracy to the BDIM formulation. Weighting functions - $\mu_0^{\epsilon,F}$ and $\mu_1^{\epsilon,F}$, are estimated during the pre-processing step in the solver. A detailed discussion of BDIM is given in [36], and its validation in the COMPSQUARE framework (on the subsonic flow past a cylinder and channel flow over sinusoidal roughness elements) is presented in [35]. It is well known that the incompressible solvers are slower than the compressible solvers as these involve solving an elliptic pressure-Poisson equation to satisfy continuity. Instead, we use a compressible flow solver and carry out the simulations at a Mach number of 0.2 ensuring that the compressibility effects are minimal. A non-dimensional time step ($\Delta t U_0/L$) of 1.5×10^{-4} is used for all the simulations. This corresponds to a CFL of approximately 1.5. The flow field, initialized with uniform values of velocity, density and pressure, has been allowed to develop until the initial transients are flushed out of the computational domain for six through flows ($t \approx 6L/U_0$). Subsequently, flow statistics are collected for 30 through flows until the turbulent quantities are converged and a statistically steady state is attained. All the simulations in this study are carried out using 2 x 32 GB V100 GPU cards. We use the standard Message Passing Interface (MPI) across the CPU processors (Intel Xeon Gold 6248 with 20 cores per socket) to communicate the information across the block interfaces. When compared to the simulations on a single CPU processor (with 20 cores), the multi-GPU implementation is $\approx 15\times$ faster for the current test case.

Table 1 Details of the test cases with Roughness

Test Cases
LRC: **L**ow **R**eynolds number **C**ase
HRC: **H**igh **R**eynolds number **C**ase
LRA: **L**ow Reynolds number **R**oughness A
HRA: **H**igh Reynolds number **R**oughness A
LRB: **L**ow Reynolds number **R**oughness B
HRB: **H**igh Reynolds number **R**oughness B

Table 2 Roughness geometry details for the test cases

Test Cases	Elements	d/L	h/L	s/L	
LRA/HRA	7	0.03	0.015	0.03	$M_{ref} = 0.2$
LRB/HRB	14	0.03	0.015	0.015	
	h/δ	Re_h	Re_D	Re_L	
LRA/LRB	0.75	280	7000	31250	$\Delta t U_0/L = 1.5 \times 10^{-4}$
HRA/HRB	1.17	610	19300	86000	

3 Results and Discussion

3.1 Grid Sensitivity and Validation

The computational grid is divided into three blocks: cavity block, upstream block comprising of the flat plate with an elliptic leading edge and roughness elements, and a downstream block where a new turbulent boundary layer develops beyond the cavity trailing edge. A six point overlap exists between the block interfaces to preserve the accuracy of the spatial discretization schemes [30]. Table 3 gives the details of the grids used in the current study. Simulations for the baseline case are carried out on two different grid resolutions: coarse grid (R_1) and fine grid (R_2) comprising of 9.4 and 38 million nodes, respectively. Apart from doubling the grid points in the span for R_2 grid, the resolution within the cavity has been increased by a factor of 2.7. For the test cases employing roughness elements, R_3 grid with 35 million nodes is employed. When compared to R_1, the resolution along the span is tripled and the grid is refined in the streamwise direction around the roughness elements (in the upstream block) to accurately resolve the geometry. Each roughness element is resolved using $38 \times 15 \times 15$ grid points in x, y, and z directions respectively resulting in approximately 8500 grid points per element. In the current simulations, it is crucial to capture the dynamics of the (a) boundary layer/shear layer behind the roughness elements, (b) shear layer separating from the cavity leading edge (c) flow within the cavity and (d) new boundary layer growth downstream of the cavity trailing edge. All these critical flow regimes are captured with fine grids without any wall functions. Hence, the eddy-resolving simulations in the current study can be classified as the wall-resolved large-eddy simulations (LES). As illustrated in Fig. 3(a) (where every fourth grid point has been shown for clarity), a gradual geometric grid stretching with a stretching factor of 1.015 has been employed in the wall-normal direction along all the walls of the cavity. This also helps in resolving the roughness elements accurately using the BDIM approach. Of the 269 points along the y-direction in the cavity block, around 230 grid points resolve the cavity region (with ≈ 100 points clustered in the shear separating from the leading edge and 130 points within the cavity). As mentioned in section 2.1, the grid is stretched beyond $y/L > 0.4$ upto the upper slip wall using 40 grid points. Similarly, around 20 grid points in the downstream block are used to stretch the grid in the streamwise direction beyond $x/L > 8.5$ to minimize any reflections from the outflow boundary.

Table 3 Grid resolution for sensitivity study

Grid	R1 ($N_x \times N_y \times N_z$)	R2 ($N_x \times N_y \times N_z$)	R3 ($N_x \times N_y \times N_z$)
Cavity	300 ×269 × 64	600 ×389 × 128	300 ×269 × 192
Upstream	153 ×150 × 64	153 ×150 × 128	368 ×150 × 192
Downstream	290 ×150 × 64	290 ×150 × 128	290 ×150 × 192

Most of the simulations in the literature inject a turbulent boundary layer at the inlet. In such simulations with fully turbulent boundary layers, the grid resolutions can be expressed in terms of wall units. However, in the current simulations, the incoming flow is laminar and undergoes transition behind the roughness. The boundary layers at the leading edge of the cavity are transitional and require long recovery lengths to exhibit typical characteristics of a fully developed turbulent boundary layer. Hence, the adequacy of grid resolution for such shear layer dominated flows (unlike the wall-bounded turbulent boundary layers) is estimated in Kolmogorov units using the scale ratio, R following Ma et al. [37] and You et al. [38]. It is defined as the ratio of the local grid-scale to the local Kolmogorov length scale as follows:

$$R = \frac{V^{1/3}}{\eta_k}, \qquad \eta_k = (\frac{\nu^3}{\epsilon})^{1/4} \tag{2}$$

Here, V is the local cell volume and η is the kolmogorov length scale. The turbulent kinetic energy dissipation ϵ is approximated as $\epsilon = P - C$, where P and C are the production and convection of turbulent kinetic energy respectively. On a coarser grid $R1$, Fig. 3(b) shows the contour plot of R estimated using the time-averaged statistics. It is evident that the value of R in the domain is well below 50, which indicates that the grid resolution is adequate enough to capture most of the turbulent kinetic energy [38]. A spanwise extent of $0.45L$ is chosen for the simulations. To verify the adequacy of spanwise extent, instantaneous velocity is recorded at three streamwise locations labelled A, B and C in Fig 3 (b). Subsequently, the autocorrelation coefficient, R_{uu}, of the streamwise velocity fluctuation $u' = u - \bar{u}$, has been estimated as follows:

$$R_{uu} = \frac{< u'(z,t)u'(z+\Delta,t) >}{< u'(z,t)u'(z,t) >} \tag{3}$$

Here, Δ is the lag in the spanwise direction and $<>$ denotes the time averaging operator. Figure 3(c) plots the spanwise two point correlations of u' for LRC at locations A, B, C. The correlation coefficient is unity at $z/L = 0$. It decays to zero with an increase in the spanwise lag, thereby demonstrating the decorrelation of the signal within the chosen spanwise extent. At a point closer to the leading edge of the cavity, the signal decorrelates at z/L ≈ 0.12. Further downstream at points B and C, the shear layer transitions to turbulence. Hence, the first zero crossings occur earlier at $z/L \approx 0.05$ as the size of the spanwise structures are smaller than those at point A. This assures that the spanwise extent of $0.45L$ is sufficient enough to accommodate all the dominant flow features formed during the flow transitioning to turbulence. In the current simulations, the typical traits of a zero pressure gradient turbulent boundary layers are only evident further downstream of the cavity trailing edge at $\approx x/L > 7$. Based on the friction velocity measured at $x/L = 7.5$,

the grid resolutions in wall-units are estimated to be $\Delta x^+ \approx 18$, $\Delta y^+ \approx 1$ and $\Delta z^+ \approx 4$ for low Reynolds number cases and $\Delta x^+ \approx 41$, $\Delta y^+ \approx 2.2$ and $\Delta z^+ \approx 10$ for the high Reynolds number cases.

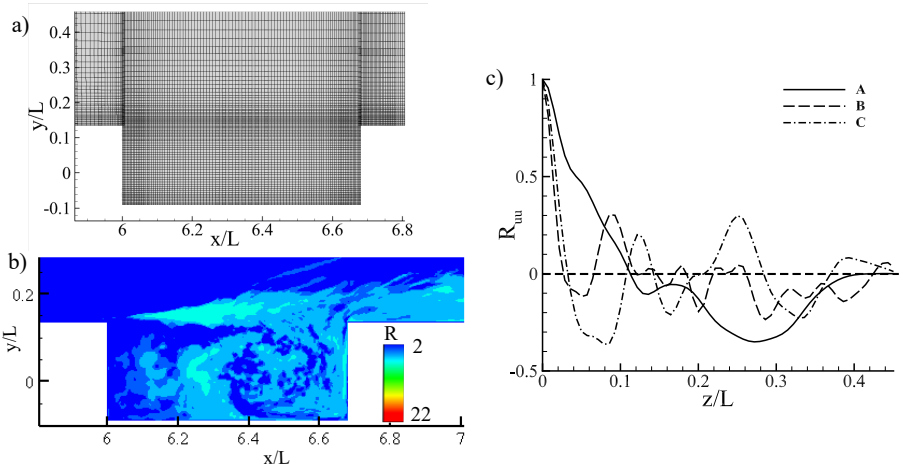

Fig. 3 a) Grid near the cavity region with every fourth grid point shown in the respective blocks for clarity (b) Contours of scale ratio R showing grid resolution in Kolmogorov units, (c) Auto-correlation, R_{uu} at points A,B,C. Locations $(x/L, y/L)$ of points A, B, C are A (6.1, 0.15), B (6.64, 0.15), C (7, 0.2).

For LRC, Figures 4 (a) and (b) show the wall-normal variation of the time-averaged streamwise velocity, $< U > /U_0$, and streamwise Reynolds stresses, $< u'u' > /U_0^2$, respectively. The profiles extracted at six streamwise locations within the cavity are shown on a carpet plot. It is evident that the results obtained on both the grids R_1 and R_2 are consistent. The difference in the streamwise Reynolds stress on both the grids is limited to $\approx 2-3\%$ demonstrating that the results are grid independent. All the results reported in this paper are simulated on the finer grid R_3 comprising of 35 million grid points with a refined resolution behind the roughness elements and along the span when compared to R_1. In the figure, we have also overlaid the experimental data from the low-speed measurements carried out at the University of Glasgow for comparison. The PIV setup used for the experiments, sampling rate, number of samples chosen for statistical convergence, and the method of processing the raw PIV images using the software package DaVis 8., LaVision (including the number of iterations and the size of interrogation window in each iteration) are the same as that described in Fujiwara et al. [21, 39]. The uncertainty in velocity was estimated to be less than 2% of the mainstream velocity. The trends of both the mean and second order statistics predicted by the eddy resolving simulations are qualitatively identical to the measurements. Consistent with the experiments, the two peak pattern of the Reynolds stresses beyond $x/L > 6.3$ has been captured. As evident from the contours of $< u'u' >$ in Fig. 4 (c), the primary peak is attributed to the turbulence

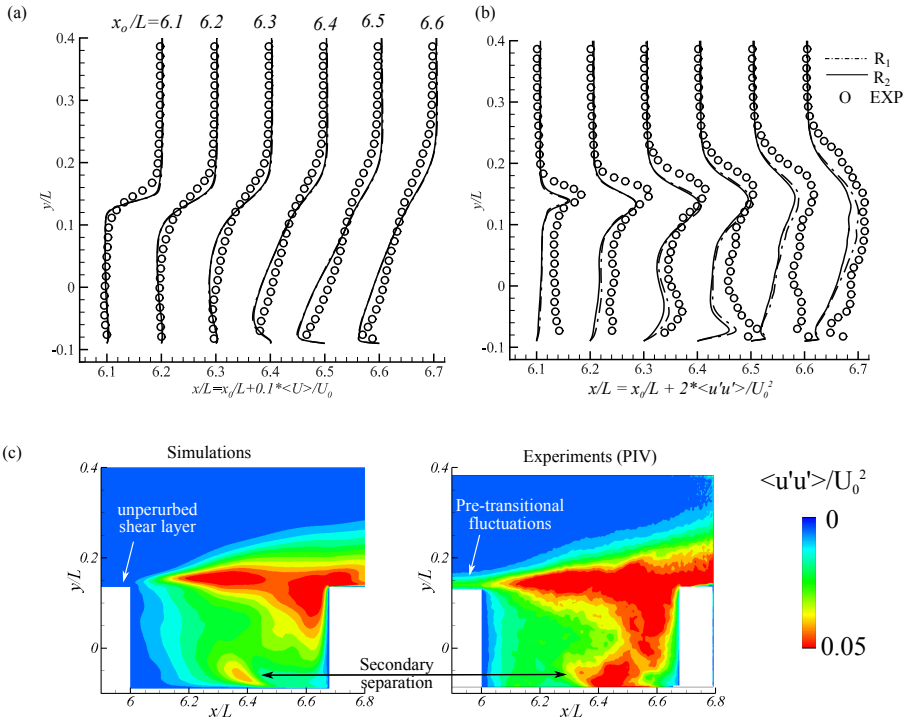

Fig. 4 Comparison of: (a) streamwise velocity and (b) Reynolds stress $< u'u' >$ for R1 and R2 grids against the experimental data. (c) Contours of $< u'u' >$ predicted by simulations and experiments for LRC.

within the destabilizing shear layer. The near-wall peak is associated with the secondary shear layer separating on the cavity floor due to the recirculating flow within the cavity. On a quantitative front, some discrepancies are notable between the PIV (Particle Image Velocimetry) and simulations which is attributed to the level of free-stream turbulence intensity (FST). As mentioned earlier, the current simulations are carried out in the absence of FST while a turbulence intensity of $2-3\%$ has been measured in the experiments. At the cavity leading edge, Fig. 4 (c) clearly demonstrates the presence of pre-transitional fluctuations in the experiments in contrast to the unperturbed flow predicted by the simulations. FST promotes bypass transition due to the breakdown of 'Klebanoff streaks' and alters the state of the boundary layer at the leading edge; subsequently affecting the transition and spreading rate of the separated shear layer. Hence, when compared to the measurements, the simulations predict a steeper gradient of the velocity profiles, relatively lower Reynolds stresses and a wall-normal shift in the location of the primary peak of $< u'u' >$ associated with the destabilizing shear layer.

3.2 Flow physics downstream of the roughness elements

In this section, we address the effect of incorporating sparse (configuration A) and densely packed (configuration B) roughness elements on the dynamics of the boundary layer developing behind the roughness up to the cavity leading edge. Coherent structures in the flow can be typically visualized iso-surfaces of Q, which is the defined as the positive second invariant of velocity gradient as follows: $Q = 0.5(\|\mathbf{\Omega}\|^2 - \|\mathbf{S}\|^2)$. Here, $\|\mathbf{\Omega}\|$ and $\|\mathbf{S}\|$ represent the norm of the vorticity and strain tensors respectively and Q represents a local balance between them [40]. Figure 5 compares the instantaneous flow features at low and high Reynolds numbers. Figure 5(a) shows the iso-surfaces of the Q-criterion coloured with the instantaneous streamwise velocity, to identify the vortical structures behind roughness elements. Figure 5(b) also shows the instantaneous contours of $y-$ vorticity on a wall-normal plane ($y/L = 0.14$) to identify the rotational sense and interaction between these streamwise vortices.

For sparsely spaced roughness (LRA, LRB), the flow approaching each of the roughness element separates at the leading edge of the element, resulting in the formation of a standing horseshoe vortex [41]. The horseshoe vortex wraps around the hemisphere generating a pair of counter-rotating streamwise vortices (see 5(b) LRA, HRA) which are referred as a horseshoe vortex pair (HP). A weak counter rotating trailing edge vortex pair (TP) can also form on the tip of the hemispherical element. The strength of these TP vortices however rapidly decays downstream. Consistent with the observations of [42], the flow separates over the roughness elements and hairpin vortices are shed from the tip. As noted in the PIV of [43] over isolated hemispherical roughness, HP vortices induce up-wash and down-wash motions in the lee of the wake resulting in the formation of low-speed and high-speed streaks respectively. The streaks induce positive and negative fluctuations of the form $\pm u'$ to the mean flow $\bar{U}$. In the context of isolated roughness elements, horseshoe pair can further trigger additional pair of streamwise vortices downstream. Nevertheless, for the distributed roughness considered here, the flow accelerates in the spacing between the distributed roughness elements. Non-linear interaction between these low-speed and high-speed streaks behind adjacent roughness elements, along with the hairpin vortices, enhances the spanwise inhomogeneity of the flow leading to bypass transition. As evident from Fig. 5(b) HRA case, the horseshoe pair is much more stronger at higher Reynolds numbers. Hence, the transition sets in earlier at a higher Reynolds number ($x/L \approx 5.8$ for HRA) than that at a lower Reynolds number ($x/L \approx 6.2$, which is beyond the cavity leading edge for LRA).

The transition behind the densely packed roughness elements (LRB, HRB) is significantly different to that behind the sparsely spaced elements. The streamwise horseshoe vortices downstream of the densely spaced elements (LRB/HRB) are remarkably weaker (see 5(b) LRB, HRB) than those observed for LRA/HRA. In fact, the flow separates all along the span behind the densely packed roughness and exhibits a transition behaviour similar to that of the flow

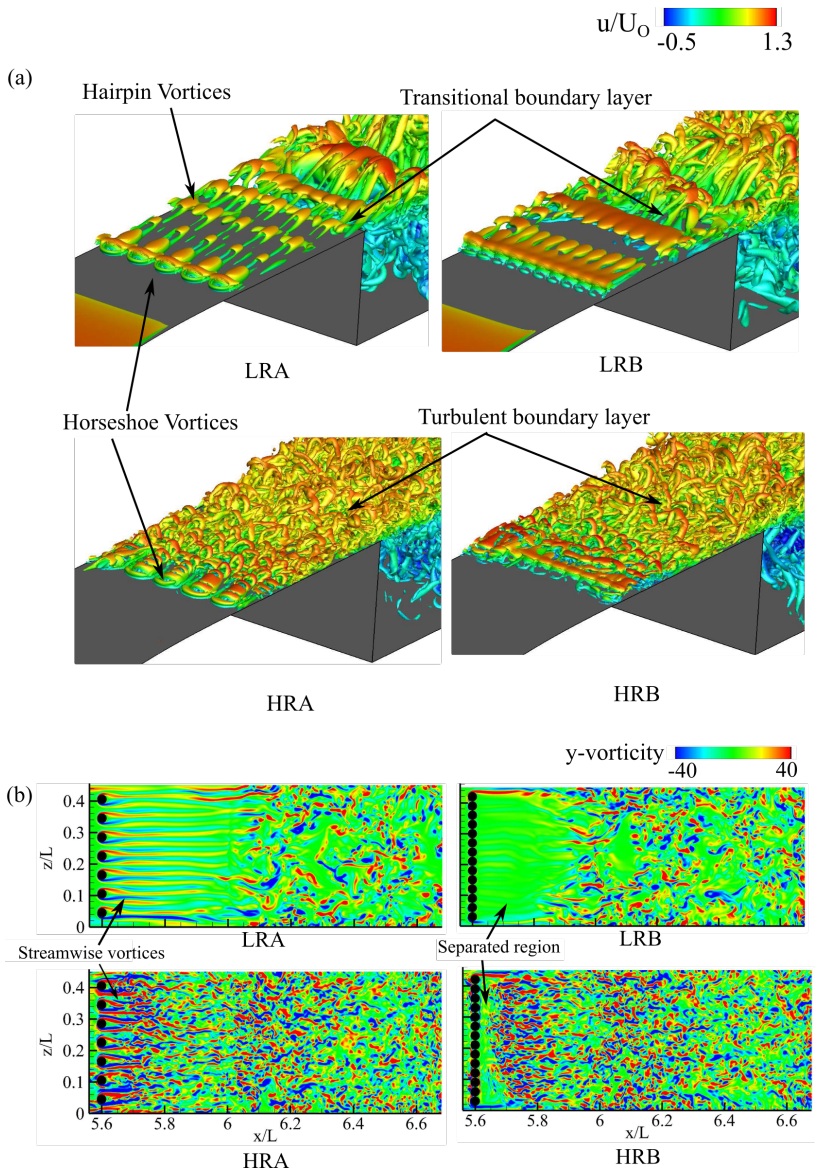

Fig. 5 Iso surfaces of Q-criterion (Q=20 for LRA, LRB and Q=150 for HRA,HRB) coloured with the streamwise velocity.

behind a 2D roughness element. A typical inviscid Kelvin-Helmholtz instability drives the transition of the separated shear layer promoting a turbulent reattachment [44]. In Figures 5(a,b), small scale structures at $x/L \approx 5.85$ for HRA and $x/L \approx 5.7$ for HRB, downstream of the separated region, indicate the instantaneous reattachment of the flow.

In literature, the separated shear layer over an isolated roughness element is observed to destabilize beyond a critical Reynolds number, $Re_{h,cr} = \rho_\infty u_B h/\mu_\infty$, where h is the height of the roughness element and u_B is the streamwise velocity at height h in the absence of roughness. Tani [45] proposed an empirical formulation for the the flow transitioning over a hemispherical element as $Re_{h,cr} = 600(h/D)^{0.4}$, where h and D are height and diameter of the hemisphere. For the roughness dimensions considered in the current study, the critical Reynolds number is estimated to be $Re_{h,cr} = 455$. As listed in Table 2, the roughness-height based Reynolds numbers, Re_h, from the current simulations are in the supercritical regime (≈ 610) for HRA and HRB while the Re_h of LRA and LRB are in the subcritical regime (≈ 280). Interestingly, all the simulations show that the flow transitions behind the distributed roughness. This discrepancy is attributed to the fact that the transition onset over distributed roughness patterns occurs earlier when compared to the isolated roughness [46].

Figure 6(a) shows the contours of the time-averaged streamwise velocity on the wall-parallel plane ($y/L = 0.14$) and wall-normal plane ($z/L = 0.225$) passing through the roughness element. Zones of negative shear, which represent the recirculating regions, are blanked out in these figures. A marginal flow separation at the leading edge of roughness is observable in all the cases. The corresponding horseshoe vortex at the leading edge is shown in the inset plots with the streamlines overlaid. The flow accelerates over windward side of the the hemisphere and separates from the surface. For LRA and HRA, a velocity deficit in the lee of of the roughness elements is evident in the $xz-$plane. Interestingly, regions of velocity deficit also exist in between the roughness elements (see LRA and HRA at $z/L = 0.2$ and 0.25). This low-speed streak results due to an up-wash motion which is induced when the clockwise rotating leg (of HP vortex pair) of a roughness element interacts with the counter-clockwise rotating leg of the adjacent element. An equivalent down-wash mechanism also results in high-speed streaks. Hence, the spanwise spacing between two successive low-speed or high-speed streaks is around $s/2$, where s is the spacing between roughness elements. In contrast to LRA/HRA, the flow separates entirely behind the densely packed elements for LRB and HRB. As noted earlier, the transition of the separated shear layer promotes turbulent reattachment ahead of the cavity. The flow reattached at $x/L \approx 5.9$ for LRB and at $x/L \approx 5.7$ for HRB, significantly reducing the extent of separation at higher Reynolds numbers. Figure 6(b) presents the streamwise evolution of the time and span-averaged skin-friction coefficient C_f. For LRB and HRB, zero-crossings S_{LRB}, S_{HRB} and R_{LRB}, R_{HRB} marked in the figure represent the flow separation and reattachment points. On the other hand, the span-averaged C_f doesn't show any indication of flow separation for sparsely spaced roughness (LRA/HRA). Downstream of the roughness ($x/L > 5.62$), the transition location can be approximated as the streamwise station beyond which an increase in C_f is observable. The transition locations for LRA, HRA and HRB are approximately between $x/L \approx 5.66 - 5.72$ while LRB transitions

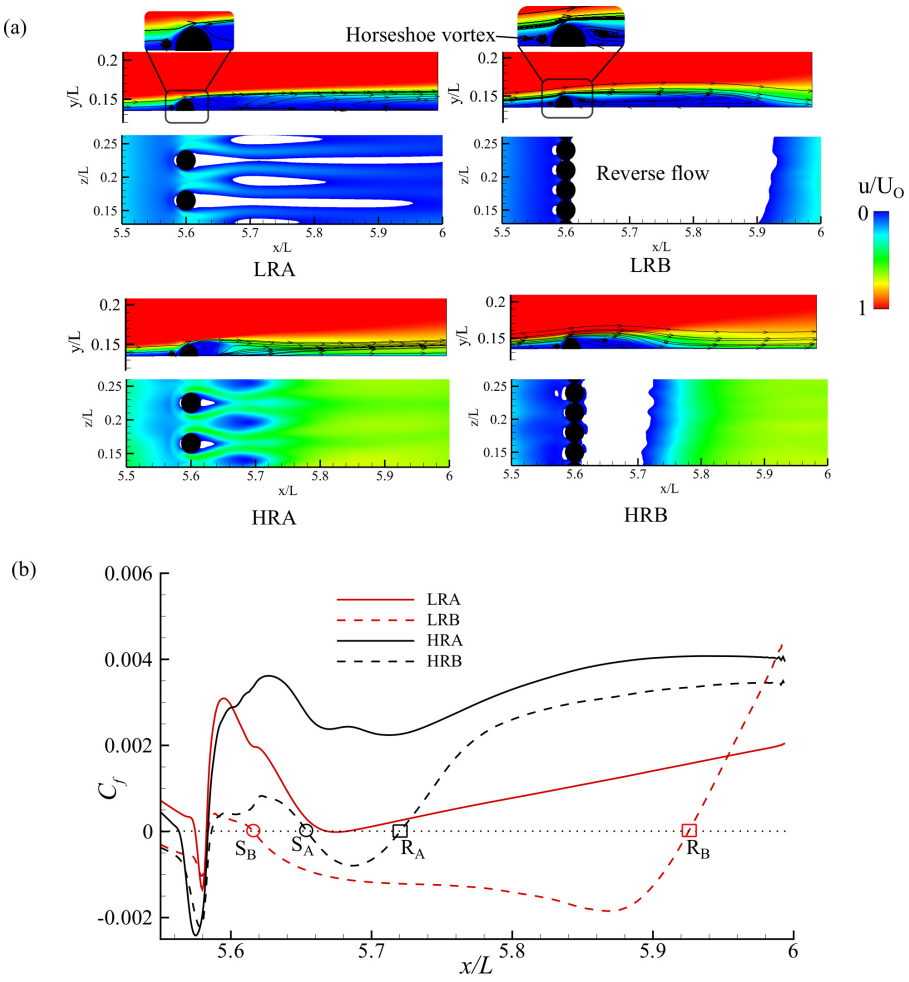

Fig. 6 (a) Contours of streamwise velocity on wall-normal ($z/L = 0.225$) and wall-parallel ($y/L = 0.14$) planes (b) Streamwise variation of skin friction coefficient for test cases with roughness.

further downstream at $x/L \approx 5.88$. The results also indicate that, despite a relatively early transition, the streamwise growth of C_f behind sparsely spaced roughness (LRA/HRA) is more gradual in contrast to a steeper C_f growth during the flow reattachment for densely spaced cases (LRB/HRB).

Figures 7 (a,b) compare the mean streamwise velocity profiles upstream of the cavity leading edge for all the test cases including those without roughness. The state of the boundary layers for LRC and HRC are laminar. However, test cases with roughness elements exhibit inflectional velocity profiles due to the shear layer separating over the roughness elements. Comparing the velocity profiles at $x/L \approx 5.7$, it is evident that the separation is stronger behind the densely spaced roughness and hence the inflection points of LRB/HRB profiles

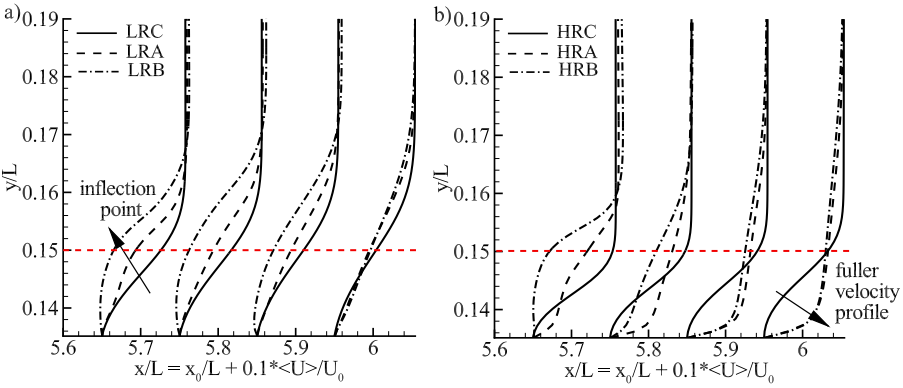

Fig. 7 Comparison of velocity profiles downstream of the roughness elements a) Low Reynolds number, b) High Reynolds number

are farther away from the wall compared to the LRA/HRA. At the leading edge of the cavity ($x/L \approx 5.95 - 6.0$), the state of the boundary layers are transitional at low Reynolds numbers (LRA/LRB). As expected, the growth of turbulent boundary layer post transition is prominent at higher Reynolds numbers (HRA/HRB). The velocity profiles are observed to be more fuller and turbulent, although still far from exhibiting the typical log-law of the wall due to a shorter recovery length behind the roughness elements. Due to enhanced mixing upstream of the cavity, thicker boundary layers are observed at the cavity leading edge. The velocity profiles of LRA/LRB and HRA/HRB are almost identical at the leading edge of the cavity. Although the spacing between the roughness elements had a marginal effect on the boundary layer thickness, it will be demonstrated in the subsequent sections that the spacing between elements has a noticeable effect on the turbulent kinetic energy and its role in suppressing the cavity tones. For LRA/LRB the boundary layer thickness is $\delta/L \approx 0.055$, which is $\approx 37.5\%$ thicker than LRC with $\delta/L \approx 0.04$. Similarly, for HRA/HRB $\delta/L \approx 0.06$, which is $\approx 50\%$ higher than HRC with $\delta/L \approx 0.03$.

3.3 Flow physics within the cavity

Shear layer instability

The state of the boundary layer (thickness & turbulence kinetic energy) at the leading edge of the cavity ($x/L = 6.0$) alters the growth of the shear layer and the recirculations within the cavity. Turbulent kinetic energy (TKE) is estimated from the time-averaged Reynolds stresses as $(\overline{u'u'} + \overline{v'v'} + \overline{w'w'})/2$, where overbar denotes averaging in time. For all the test cases, Fig. 8 (a) shows the contours of time and span averaged TKE and Figures 8(b,c) compare the streamwise variation of the maximum TKE within the cavity. For the baseline cases (LRC, HRC), the growth of TKE can be classified into three

distinguishable regions R-I, R-II and R-III. In R-I ($x/L < 6.1$), the TKE value increases gradually where the shear layer, although predominantly laminar, is under the influence of the flow entrainment from the recirculating vortical flow within the cavity. In R-II ($6.1 < x/L < 6.4$), transition of the shear layer results in a rapid growth of TKE. It reaches a peak value of ≈ 0.08 at $x/L \approx 6.4$ for LRC while it saturates earlier for HRC at $TKE \approx 0.07$ and $x/L \approx 6.3$. In this zone, Bres [7] notes that the shear layer exhibits an approximate linear growth with a constant spreading rate [1]. R-III corresponds to a fully turbulent state where the TKE gradually decreases owing to its diffusion in wall-normal and spanwise directions. At the trailing edge of the cavity ($x/L = 6.8$), a notable growth of TKE is evident due to the impingement of vortical structures on the aft wall.

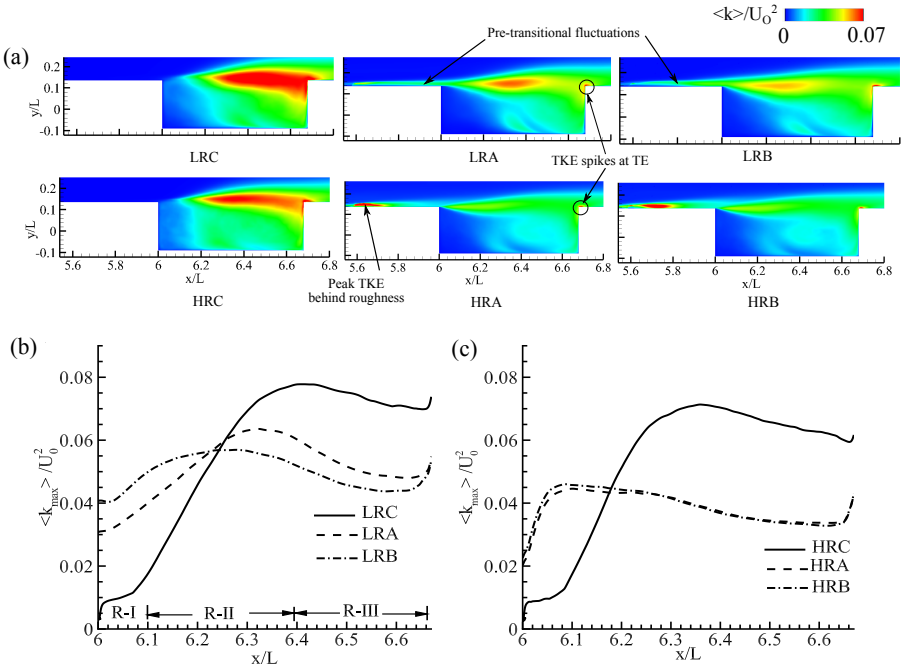

Fig. 8 (a) Comparison of the contours of turbulent kinetic energy (TKE) for all the test cases. Streamwise variation of maximum TKE within the cavity at (b) low Reynolds number and (c) high Reynolds number.

With distributed roughness elements, Figure 8(a) shows higher TKE levels between $5.6 < x/L < 6$ upstream of the cavity leading edge. At higher Reynolds numbers (HRA/HRB), local spike in the TKE contours behind the roughness elements is also observable between $5.6 < x/L < 5.8$. R-I is entirely bypassed in these cases due to enhanced TKE levels at the cavity leading edge. Both LRA and LRB show an earlier onset of non-linearity and

[1] Spreading rate is typically defined as $d\delta_w/dx$, where δ_w is the vorticity thickness

breakdown of shear layer when compared to LRC; with LRB transitioning relatively earlier than LRA. Similar upstream shift in the peak k_{max} is observed at higher Reynolds numbers (HRA/HRB) when compared to the baseline HRC. Recall from Figure 7(b) that the velocity profiles at the cavity leading edge are similar for both HRA/HRB. Hence, identical TKE distributions are observable for both HRA/HRB suggesting that the effect of roughness configurations (sparse/dense spacing) has minimal impact on the dynamics at higher Reynolds numbers. For all the test cases with roughness, a significant reduction in the TKE is notable beyond $x/L > 6.2$ both within the cavity, on the cavity floor and at the trailing edge. When compared to LRC, the peak k_{max} decreased by $\approx 18\%$ for LRA and $\approx 30\%$ for LRB. At higher Reynolds numbers, the peak k_{max} of HRA/HRB reduced by $\approx 35\%$ when compared to HRC. In LRC/HRC large scale spanwise coherent vortices impinge on the aft wall of the cavity at trailing edge. When roughness elements are employed upstream of the cavity, the spanwise coherence of these spanwise vortices is significantly reduced and smaller flow structures impinge on the cavity aft wall (see $x/L = 0.68$ in Fig. 5(b)). Apart from reduction the turbulence levels, loss in spanwise coherence has implications on the shear layer instabilities (Rossiter modes) and the tonal noise produced in the cavity. These aspects will be discussed in detail in the subsequent sections.

Centrifugal instability

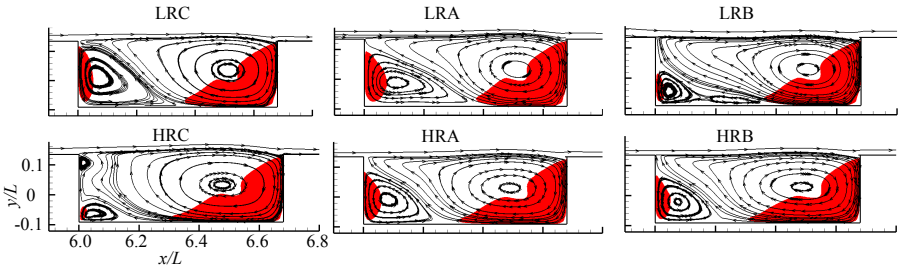

Fig. 9 Streamlines showing the recirculation regions within the cavity. Contours of Rayleigh discriminant exceeding threshold value of $\eta_R(x, y) > 5\%$ are overlaid.

Through linear stability analysis, Bres [7] demonstrated the existence of low frequency 3D hydrodynamic instabilities. These are found to arise from global centrifugal instabilities associated with the recirculations within cavity. The cavity walls decrease the momentum of outer streamlines of the recirculating flow [7] resulting in a reduction in the angular velocity from the centre of the recirculation zone towards the wall. Hence, a centrifugal force develops in the radial direction which can lead to the onset of centrifugal instability. The effect of roughness on the regions susceptible to centrifugal instability (CI) has been investigated. Figure 9 compares the time and span averaged streamline

patterns within the cavity for all the test cases. Rayleigh discriminant can be used to capture the regions prone to CI, which is defined as follows [7]:

$$\eta_R(x,y) = -\frac{\partial||\mathbf{r}(x,y)\times\mathbf{V}(x,y)||^2}{\partial r} \tag{4}$$

Here, $\mathbf{r}(x,y) = (x-x_c, y-y_c)$ is the radius vector; (x_c, y_c) being the location of the minimum velocity inside recirculation region; and $\mathbf{V}(x,y)$ is the velocity vector. In the inviscid limit, the regions with positive values of Rayleigh discriminant indicate the presence of CI. Following Bres [7], we have overlaid the contours (marked in red) of the $\eta_R(x,y)$ exceeding 5% of the maximum value in Figure 9. In all the test cases, except HRC, two recirculating regions (primary/secondary) are observable within the cavity. For HRC, the primary circulation is significantly larger than that of LRC thereby shrinking the second circulation. Interestingly, for HRC small recirculation is also observed at the leading edge of the cavity. The size of these recirculations is sensitive to the initial spreading of the shear layer and reverse flow velocities within the cavity. It is evident that both the recirculating regions are prone to CI while interacting with the cavity walls. However, roughness has a minimal impact on the extent of the unstable zone associated with the primary recirculation. At low Reynolds numbers, the primary recirculation for LRA and LRB is relatively larger than LRC, thereby shrinking the secondary recirculation at the upstream wall of the cavity. Hence, the instability associated with the secondary recirculation is bound to diminish for LRA/LRB; with the reduction being more pronounced for LRB when compared LRA. Nevertheless, at higher Reynolds numbers, the primary/secondary circulation patterns of both HRA/HRB and the corresponding zones susceptible to CI are identical.

Flow control due to roughness

In cavities, large pressure fluctuations are notable (a) in the shear layer evolving from the cavity leading edge and (b) near the cavity trailing edge where the spanwise coherent structures impinge on the aft wall [11]. As discussed in the introduction, several active and passive flow control strategies have been developed towards suppressing these pressure fluctuations (and the associated 'cavity tones') within the cavity. In this section, we address the efficacy of sparse and densely packed roughness elements towards reducing the cavity tones.

To facilitate the time series analysis, unsteady pressure fluctuations are recorded at several locations within the cavity. The data is recorded for $\approx 30L/U_0$ with a non-dimensional time step of $\Delta t U_0/L = 1.5\times10^{-4}$. An inset plot in Figure 10 shows selected probes $P1, P2, P3$ placed in the shear layer and the primary recirculation. In addition, pressure fluctuations are recorded at the trailing edge P_{TE} and on the cavity floor P_F. The power spectral density (PSD) of these fluctuations is estimated using Welch's method. A Hanning window with 50% overlap between the samples is used to generate the PSD.

Subsequently, the pressures in the frequency domain are converted to sound pressure levels (SPL) in decibels (dB) as follows:

$$SPL = 10log_{10}\left(\frac{PSD}{P_{ref}^2}\right) \tag{5}$$

where P_{ref} is the reference pressure of 2×10^{-5} Pa [47].

Figure 10 compares the sound pressure spectra at probes $P1$, $P2$, $P3$ and P_{TE} for all the test cases at low and high Reynolds numbers. Note that the Strouhal number is defined as fL_c/U_∞ based on the length of the cavity L_c and free-stream velocity U_∞ to facilitate comparison against the empirical correlations of Rossiter modes. Here, cavity length L_c is the distance between the leading and trailing edges of the cavity, which is equal to 0.68L (See Figure 1). For the baseline cases, LRC and HRC, distinct peaks are observable in the SPL spectra which correspond to the different Rossiter modes widely addressed in the literature [7, 11]. These modes are a result of the cavity resonance due to the reinforcement of the instabilities in the shear layer at the leading edge and the upstream travelling pressure waves at the cavity trailing edge due to vortex impingement [48]. The predicted frequencies of the two Rossiter modes are $St \approx 0.35$ and 1.0. Rossiter [8] proposed a semi-empirical formulation to predict the Strouhal number of these modes as follows:

$$St_{Lc} = \frac{fL_c}{U} = \frac{n-\alpha}{M+1/\kappa} \tag{6}$$

where $\alpha = 0.25, 1/\kappa = 1.75$ and n=1,2,3... denote different modes. For n=1,4 and M=0.2, the theoretical Strouhal numbers are 0.38 and 0.9 respectively which are in favorable agreement with those obtained from the simulations. The frequency of the fundamental cavity mode corresponding to the peak SPL is $St \approx 1.0$ which is the second Rossiter mode (n = 2) which is inline with the observations of Sun et al. [11]. This frequency is predominantly observable at all the probe locations.

Figure 10 clearly demonstrates that the inclusion of roughness elements resulted in a noticeable drop in the SPL levels at probes $P2$, $P3$ and P_{TE} at both the Reynolds numbers. The drop in SPL is more prominent at lower frequencies $0.1 < St < 10.0$. The cavity tones associated with Rossiter modes are effectively suppressed at these locations. As noted in the previous section, suppression of the Rossiter modes is attributed to the mixing promoted by the upstream distributed roughness elements which alter the shear layer stability characteristics. The coherence of the spanwise vortices is significantly reduced and smaller flow structures impinge on the cavity aft wall, disrupting the feedback between the acoustic waves from cavity trailing edge and the shear layer shedding. Similar observations were made by Vakili and Wolfe [18] who examined the active suppression of cavity tones through mass-injection at the cavity leading edge. Infact, Yokoyama et al. [49] reported a reduction in the cavity tones by reducing the spanwise coherence of the shear layer rollers with elevated levels of free-stream turbulence. Despite a reduction of the tonal noise

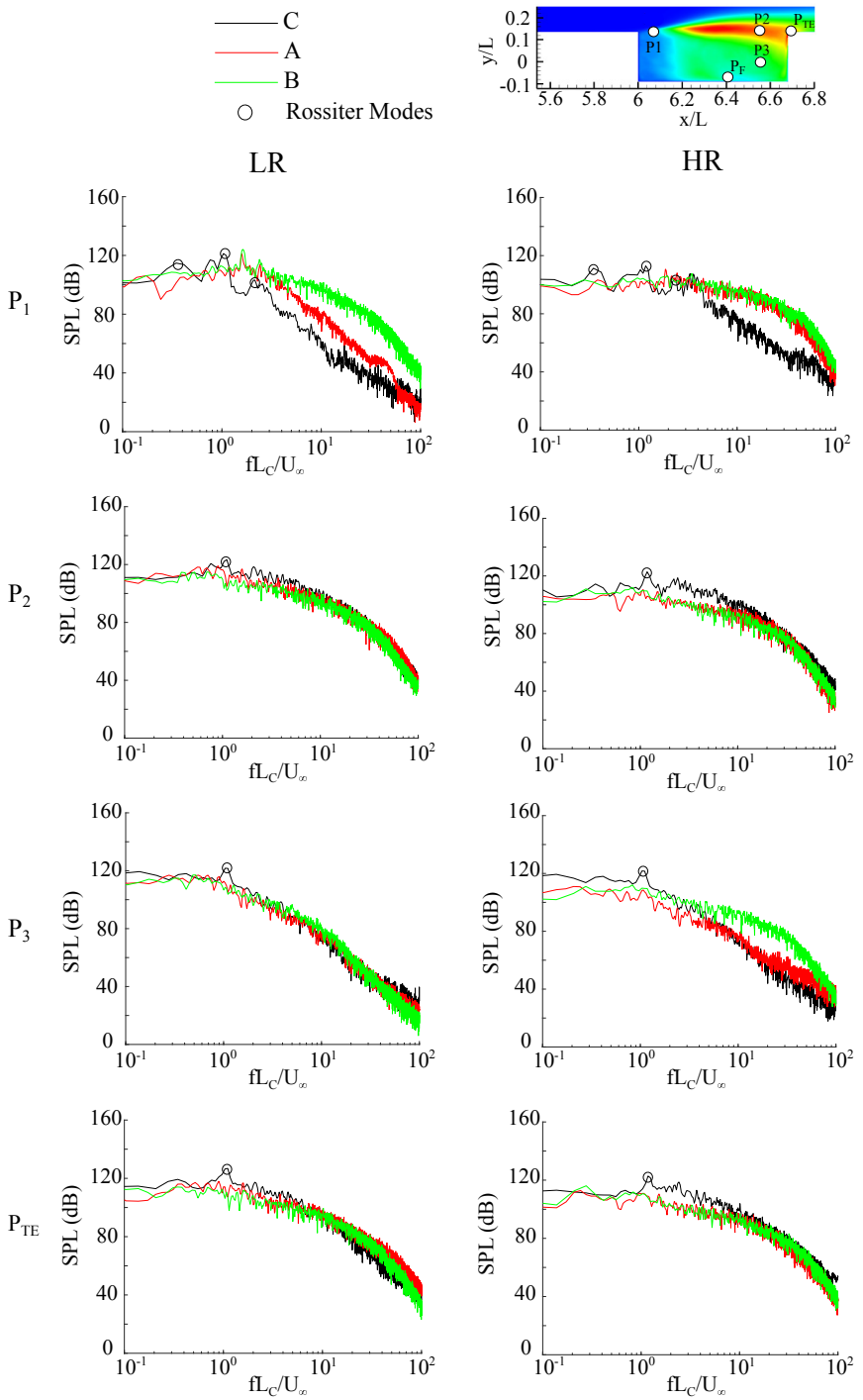

Fig. 10 Comparison of the sound pressure level (SPL) spectra at different probe locations. C/A/B correspond to the test cases without/sparse/dense roughness elements. LR and HR correspond to low and high Reynolds number cases. Probe locations $(x/L, y/L)$ on the midplane $z/L = 0.225$: P1 (6.1,0.15), P2 (6.54, 0.15), P3 (6.54, 0.007), $\mathrm{P}_F(6.41, -0.08)$, $P_{TE}(6.65, 0.15)$

at low frequencies ($0.1 < St < 10$), an increase in the SPL is notable from the plot at higher frequencies ($10 < St < 100$). In particular, the broadband noise at P1 (and at P3 for high Reynolds number) has significantly increased with roughness elements. A SPL spike is observable for LRA and LRB at $St \approx 1.5$ in contrast to $St \approx 1.0$ for LRC. At probe P_{TE}, a marginal increase in the broadband SPL is observed for LRA/LRB. These observations finds support from the studies of Baysal et al. [17], who attributes the increase in the broadband noise to the redistribution of the spectral energy from low-frequency tonal peaks to higher broadband frequencies. Recall from Fig. 8(b) that LRB transitioned earlier than LRA while the TKE distributions of both HRA and HRB are identical. Hence, the broadband noise of densely spaced roughness (LRB) at P1 is higher than that of LRA while that of HRA and HRB are almost similar.

In contrast to the Fourier transform, Continuous Wavelet Transform (CWT) is a useful tool which provides more information of the localized events in strongly non-linear regions in a time-frequency domain. Figures 11(a,b) illustrate the CWT of the pressure fluctuations recorded at probes $P1$ and P_{TE} respectively. For the baseline cases, the frequency bands corresponding to the Rossiter modes are marked with red circles. At probe P1, the wavelet energy is largely confined in the lower frequency bands. In contrast, at probe P_{TE} a significant increase in the wavelet energy is evident in the frequency bands between $1 < St < 10$ due to the impingement of large scale vortices at the trailing edge. With roughness elements, at both the probe locations, a significant reduction in the wavelet energy associated with the Rossiter modes is evident for all the cases. The reduction of wavelet energy is more remarkable at P_{TE} than at P1, particularly at high Reynolds numbers. For LRA/LRB, an upward shift in the dominant frequency band to $St \approx 1.5$ and an increase in the wavelet energy at higher frequencies when compared to LRC is observable. It indicates an increase in the broadband noise despite a reduction in the cavity tones. The plots also show that at higher Reynolds numbers, the roughness distribution (A/B) seems to have a minimal impact on the CWT. However, at low Reynolds numbers, the reduction of wavelet energy at P_{TE} is higher for LRB than LRA.

Figures 12 (a,b) compare the pressure fluctuation histories recorded at the cavity trailing edge. Low frequency high amplitude oscillations are notable for the baseline cases LRC/HRC. With roughness, a decrease in the amplitude of pressure fluctuations and a relative increase in the high frequency spectral content is evident. This is attributed to an enhanced cascading of energy to finer turbulent scales in the presence of roughness elements. These small scale structures (with high-frequency and low-amplitude spectral content) generate lower noise when impinging at the trailing edge. The decrease in amplitude of fluctuations is more notable at higher Reynolds numbers (HRA/HRB).

Following Baysal [17], we have estimated the following metrics to further assess the aeroacoustic environment: RMS of pressure fluctuations p'_{rms}, RMS

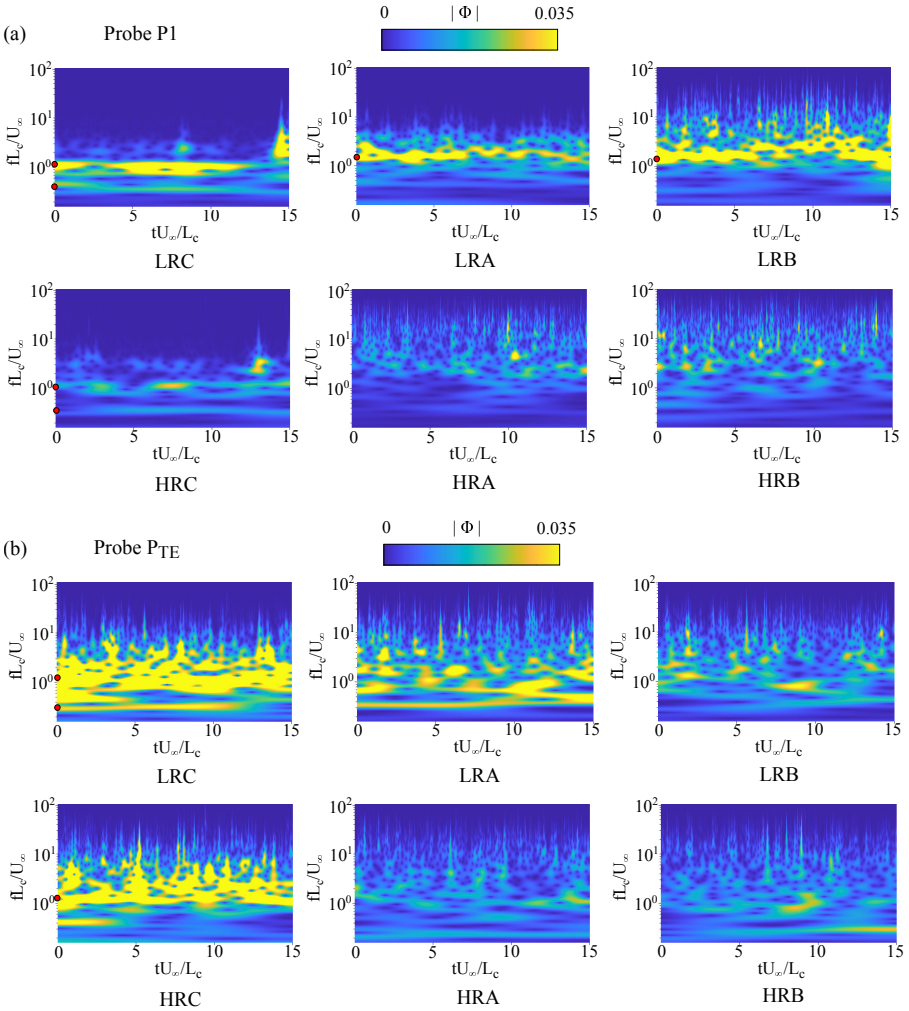

Fig. 11 Scalogram comparing the contours of the magnitude of continuous wavelet transform of unsteady pressure measured at (a) probe P1 and (b) the trailing edge P_{TE}, of the cavity.

of sound pressure levels SPL_{rms} and the maximum ratio of pressure fluctuations, $\Delta p'_{max} = max(|p'|/\bar{p})$, where $\bar{p}$ is the time-averaged pressure. Table 4 lists the values of these metrics for the pressure histories recorded at the trailing edge and on the cavity floor (see Fig. 10 for probe locations). SPL_{rms} has been estimated for the frequency ranging between $0.1 < St < 100$. We have also reported $SPL_{rms,St<10}$ for frequencies between $0.1 < St < 10$ to demonstrate the benefits of roughness towards suppressing the low-frequency cavity modes.

On the cavity floor and at the trailing edge, $\Delta p'_{max}$, which is related to acoustic energy, and p'_{rms} reduced by 40−65% with roughness. At low Reynolds

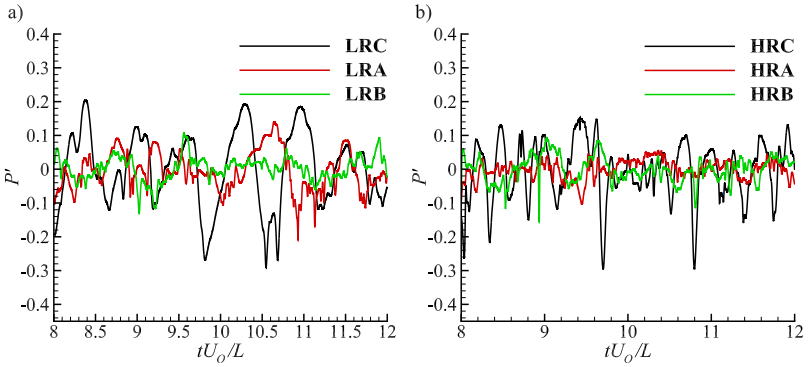

Fig. 12 Temporal variation of the pressure fluctuations at the trailing edge of the cavity

numbers, the drop is relatively higher for densely spaced roughness (configuration B) while at high Reynolds numbers, the sparsely spaced roughness (configuration A) has effectively reduced the peak and RMS pressure fluctuations. Sound pressure levels recorded on the cavity floor are almost 10 dB lower than those at the trailing edge. RMS of the SPLs recorded over a wider frequency range show a consistent reduction of 4-6 dB on the cavity floor. However, at the trailing edge, SPL reduction of 2-4 dB is observable only at higher Reynolds numbers. At low Reynolds numbers, the SPL has infact increased by 3-7 dB. The reason for this increase is evident from the spectra at P_{TE} (see Fig. 10). For LRA/LRB, although roughness has effectively suppressed the cavity tones at low frequencies, an increase in the broadband noise is notable. In contrast, SPL_{rms} estimated in the frequency range $0.1 < St < 10$ show a consistent reduction in the sound pressure levels. Densely spaced roughness show a 10-13 dB reduction of SPL_{rms} on the cavity floor and a 5-13 dB reduction at the trailing edge. In contrast, sparsely spaced roughness seem to be less effective, with SPL reducing by around 2-7 dB on cavity floor and by 3-8 dB at the trailing edge. It is also worth noting that, the efficacy of roughness elements (A/B) in reducing SPL is much more remarkable at higher Reynolds numbers for all the cases. To summarize, the roughness elements can act as passive flow control devices towards effectively suppressing the cavity tones. Also, the densely packed roughness elements seem to be more effective in suppressing the pressure fluctuations when compared to the sparsely spaced ones.

4 Conclusion

Effects of three-dimensional (3-D) distributed roughness elements on the flow characteristics within a cavity are investigated using a series of high-fidelity eddy-resolving simulations. The cavity flows generate undesirable low-frequency pressure fluctuations due to the vortex impingement over the trailing edge of the cavity. We have explored the possibility of employing distributed hemispherical roughness elements, modelled using the Boundary Data

Table 4 Comparison of RMS of pressure fluctuations and sound pressure levels at probes located at trailing edge and the cavity floor.

Probe on cavity floor				
Test Case	$\Delta p'_{max}$	p'_{rms}	SPL_{rms}	$SPL_{rms,St\leq 10}$
LRC	0.0095	0.0529	51.3	96.4
LRA	0.0051	0.0226	50.5	94.8
LRB	0.0035	0.0187	45.1	86.7
HRC	0.0055	0.0338	61.3	94.8
HRA	0.0023	0.0114	56.5	88.2
HRB	0.0033	0.0137	57.4	81.6
Probe at trailing edge				
Test Case	$\Delta p'_{max}$	p'_{rms}	SPL_{rms}	$SPL_{rms,St\leq 10}$
LRC	0.0301	0.1184	64.0	105.9
LRA	0.0126	0.0577	71.3	102.8
LRB	0.0114	0.0391	67.0	100.5
HRC	0.0259	0.0804	73.4	106.4
HRA	0.0084	0.0306	67.5	98.5
HRB	0.0088	0.0337	69.1	93.2

Immersion Method, as a passive flow control strategy towards suppressing these pressure fluctuations. A rectangular cavity with a length to depth ratio, L/D, of 3 is considered. Simulations are carried out at a Mach number of 0.2 and Reynolds numbers of 7000 and 19300, based on the free-stream velocity and the depth of the cavity. A grid sensitivity study has been carried out and the framework has been validated against the measurements/empirical correlations. Effects of sparsely and densely packed roughness elements on the stability of shear layer separating from the cavity are brought out.

Through instantaneous and time-averaged flow fields (mean and turbulence statistics), it has been shown that the pre-transitional fluctuations generated by the roughness elements: (a) resulted in transitional/turbulent flow at the cavity leading edge for low/high Reynolds numbers (b) promoted an earlier breakdown of the large-scale coherent structures in the shear layer (c) affected the size of primary and secondary recirculations within the cavity and the zones susceptible to centrifugal instability. Unsteady pressure signals, recorded at several locations in the cavity, were used the assess the aeroacoustic environment through spectral analysis (SPL spectra/wavelet transforms). The coherence of the spanwise vortices has significantly reduced with roughness. Smaller flow structures impinge on the cavity aft wall disrupting the feedback between the acoustic waves from cavity trailing edge and the shear layer shedding.

With roughness, the sound pressure levels (SPL) associated with the 'cavity tones' due to the Rossiter modes reduced by 5-13 dB. The reduction in SPL is much more prominent at higher Reynolds numbers, and with dense spacing between the roughness elements. At low Reynolds numbers, the benefit obtained by suppressing the 'cavity tones' can get eclipsed with an increase in

the broadband noise. Despite a marginal increase in the broadband noise, the suppression of high-amplitude cavity tones is beneficial in several applications like minimizing the structural vibrations in landing gear/weapon bays, controlling the dynamics in cavity flameholders, etc. The efficacy of distributed roughness elements in reducing SPL is comparable to the other flow control strategies like ramps/spoilers/mass injection upstream of the cavity.

Acknowledgments. The authors wish to acknowledge P G Senapathy Centre, IIT Madras for the computing resources, Department of Science and Technology-Science and Engineering Research Board (DST-SERB) for funding the project and NVIDIA for generously donating Quadro P6000 GPU card. The support and the resources provided by PARAM Sanganak under the National Supercomputing Mission, Government of India are gratefully acknowledged.

Declarations

The authors declare that they have no conflict of interest.

References

[1] Martin, R., Soria, M., Lehmkuhl, O., Gorobets, A., Duben, A.: Noise radiated by an open cavity at low mach number: Effect of the cavity oscillation mode. International Journal of Aeroacoustics **18**(6-7), 647–668 (2019)

[2] Gloerfelt, X., Bailly, C., Juvé, D.: Direct computation of the noise radiated by a subsonic cavity flow and application of integral methods. Journal of sound and vibration **266**(1), 119–146 (2003)

[3] Larchevêque, L., Sagaut, P., Lê, T.-H., Comte, P.: Large-eddy simulation of a compressible flow in a three-dimensional open cavity at high reynolds number. Journal of Fluid Mechanics **516**, 265–301 (2004)

[4] Erbig, L., Maihöfer, M.: A hybrid rans/les for automotive gap noise simulations. In: 25th AIAA/CEAS Aeroacoustics Conference, p. 2445 (2019)

[5] Naudascher, E., Rockwell, D.: Flow-induced vibrations: an engineering guide. Dover Publications Inc. (2012)

[6] Jackson, T.R., Haggerty, R., Apte, S.V., O'Connor, B.L.: A mean residence time relationship for lateral cavities in gravel-bed rivers and streams: Incorporating streambed roughness and cavity shape. Water resources research **49**(6), 3642–3650 (2013)

[7] Bres, G.A.: Numerical simulations of three-dimensional instabilities in cavity flows. PhD thesis (2007)

[8] Rossiter, J.: Wind-tunnel experiments on the flow over rectangular cavities at subsonic and transonic speeds. Aero. Res. Counc. (1964)

[9] Colonius, T., Basu, A., Rowley, C.: Numerical investigation of the flow past a cavity. In: 5th AIAA/CEAS Aeroacoustics Conference and Exhibit, p. 1912 (1999)

[10] Meseguer-Garrido, F., De Vicente, J., Valero, E., Theofilis, V.: On linear instability mechanisms in incompressible open cavity flow. Journal of Fluid Mechanics **752**, 219 (2014)

[11] Sun, Y., Liu, Q., Cattafesta III, L.N., Ukeiley, L.S., Taira, K.: Effects of sidewalls and leading-edge blowing on flows over long rectangular cavities. AIAA journal **57**(1), 106–119 (2019)

[12] Ganesh, N., Ananth, S.M., Nagabhushana Rao, V., Sriram, R., Kontis, K.: Eddy resolving simulations of shear layer instabilities in open cavity flows. In: Proceedings of the 8th International and 47th National Conference on Fluid Mechanics and Fluid Power (FMFP) (2020)

[13] Sun, Y., Taira, K., Cattafesta III, L.N., Ukeiley, L.S.: Biglobal instabilities of compressible open-cavity flows. arXiv preprint arXiv:1706.00300 (2017)

[14] Rowley, C.W., Colonius, T., Basu, A.J.: On self-sustained oscillations in two-dimensional compressible flow over rectangular cavities. Journal of Fluid Mechanics **455**, 315–346 (2002)

[15] Lin, K.-C., Jackson, K., Behdadnia, R., Jackson, T.A., Ma, F., Yang, V.: Acoustic characterization of an ethylene-fueled scramjet combustor with a cavity flameholder. Journal of Propulsion and Power **26**(6), 1161–1170 (2010)

[16] Heller, H., Bliss, D.: The physical mechanism of flow-induced pressure fluctuations in cavities and concepts for their suppression. In: 2nd Aeroacoustics Conference, p. 491 (1975)

[17] Baysal, O., Yen, G.-W., Fouladi, K.: Navier-stokes computations of cavity aeroacoustics with suppression devices (1994)

[18] Vakili, A., Wolfe, R., Nagle, T., Lambert, E.: Active control of cavity aeroacoustics in high speed flows. In: 33rd Aerospace Sciences Meeting and Exhibit, p. 678 (1995)

[19] Wang, Y., Li, S., Yang, X.: Numerical investigation of the passive control of cavity flow oscillations by a dimpled non-smooth surface. Applied Acoustics **111**, 16–24 (2016)

[20] Nampelly, G., Sivaramakrishnan Malathi, A., Vadlamani, N.R., Rengarajan, S., Kontis, K.: Surface roughness benefits in open cavity flows. In: AIAA SCITECH 2022 Forum, p. 0473 (2022)

[21] Sriram, R., de Isla, S.R., Lo, K.H., Kontis, K.: Cavity flow control using dielectric barrier discharge. In: 14th International Conference on Fluid Control, Measurements, and Visualization (FLUCOME), University of Notre Dame, Indiana, USA (2017)

[22] Lo, K.H., Kontis, K.: Flow around an articulated lorry model. Experimental Thermal and Fluid Science **82**, 58–74 (2017)

[23] Krist, S.L.: CFL3D User's Manual (version 5.0). National Aeronautics and Space Administration, Langley Research Center, ??? (1998)

[24] Rizzetta, D.P., Visbal, M.R.: Large-eddy simulation of supersonic cavity flowfields including flow control. AIAA journal **41**(8), 1452–1462 (2003)

[25] Gaitonde, D.V., Visbal, M.R.: High-order schemes for navier-stokes equations: algorithm and implementation into fdl3di. Technical report, Air Force Research Lab Wright-Patterson AFB OH Air Vehicles Directorate (1998)

[26] Matsuura, K., Kato, C.: Large-eddy simulation of compressible transitional flows in a low-pressure turbine cascade. AIAA journal **45**(2), 442–457 (2007)

[27] Visbal, M.R., Gaitonde, D.V.: Very high-order spatially implicit schemes for computational acoustics on curvilinear meshes. Journal of Computational Acoustics **9**(04), 1259–1286 (2001)

[28] Visbal, M.R., Gaitonde, D.V.: On the use of higher-order finite-difference schemes on curvilinear and deforming meshes. Journal of Computational Physics **181**(1), 155–185 (2002)

[29] Vadlamani, N.R., Tucker, P.G., Durbin, P.: Distributed roughness effects on transitional and turbulent boundary layers. Flow, Turbulence and Combustion **100**(3), 627–649 (2018)

[30] Visbal, M.R., Gaitonde, D.V.: High-order-accurate methods for complex unsteady subsonic flows. AIAA journal **37**(10), 1231–1239 (1999)

[31] Achu, S., Vadlamani, N.R.: Entropically damped artificial compressibility solver using higher order finite difference schemes on curvilinear and deforming meshes. In: AIAA Scitech 2021 Forum, p. 0634 (2021)

[32] Vaid, A., Vadlamani, N.R., Sivaramakrishnan Malathi, A.: Dynamics of bypass transition with roughness and pulses of free-stream turbulence. In: AIAA SCITECH 2022 Forum, p. 0453 (2022)

[33] Lin, Y., Vadlamani, R., Savill, M., Tucker, P.: Wall-resolved large eddy simulation for aeroengine aeroacoustic investigation. The Aeronautical Journal **121**(1242), 1032–1050 (2017)

[34] Vadlamani, N., Tucker, P.: Eddy resolving simulations of intake under crosswinds. Direct and Large-Eddy Simulation XI, Springer, 523–529 (2019)

[35] Sivaramakrishnan Malathi, A., Nardini, M., Vaid, A., Vadlamani, N.R., Sandberg, R.D.: On the efficacy of riblets toward drag reduction of transitional and turbulent boundary layers. In: AIAA SCITECH 2022 Forum, p. 0472 (2022)

[36] Schlanderer, S.C., Weymouth, G.D., Sandberg, R.D.: The boundary data immersion method for compressible flows with application to aeroacoustics. Journal of computational Physics **333**, 440–461 (2017)

[37] Ma, Y., Cui, J., Vadlamani, N.R., Tucker, P.: Effect of fan on inlet distortion: Mixed-fidelity approach. AIAA journal **56**(6), 2350–2360 (2018)

[38] You, D., Wang, M., Moin, P., Mittal, R.: Large-eddy simulation analysis of mechanisms for viscous losses in a turbomachinery tip-clearance flow. Journal of Fluid Mechanics **586**, 177–204 (2007)

[39] Fujiwara, K., Sriram, R., Kontis, K.: Experimental investigations on the sharp leading-edge separation over a flat plate at zero incidence using particle image velocimetry. Experiments in Fluids **61**(9), 1–21 (2020)

[40] Jeong, J., Hussain, F.: On the identification of a vortex. Journal of fluid mechanics **285**, 69–94 (1995)

[41] Klebanoff, P., Cleveland, W., Tidstrom, K.: On the evolution of a turbulent boundary layer induced by a three-dimensional roughness element. Journal of Fluid Mechanics **237**, 101–187 (1992)

[42] Acarlar, M., Smith, C.: A study of hairpin vortices in a laminar boundary layer. part 1. hairpin vortices generated by a hemisphere protuberance. Journal of Fluid Mechanics **175**, 1–41 (1987)

[43] Ye, Q., Schrijer, F.F., Scarano, F.: Geometry effect of isolated roughness on boundary layer transition investigated by tomographic piv. International Journal of Heat and Fluid Flow **61**, 31–44 (2016)

[44] Rao, V.N., Jefferson-Loveday, R., Tucker, P.G., Lardeau, S.: Large eddy simulations in turbines: influence of roughness and free-stream turbulence. Flow, turbulence and combustion **92**(1), 543–561 (2014)

[45] Tani, I.: Boundary-layer transition. Annual Review of Fluid Mechanics **1**(1), 169–196 (1969)

[46] Reda, D.C.: Review and synthesis of roughness-dominated transition correlations for reentry applications. Journal of spacecraft and rockets **39**(2), 161–167 (2002)

[47] Aylı, E., Yılmaz, İ., Selin, A.: Numerical analysis of supersonic cavity flow. In: 6th International Conference on Thermal Engineering Theory and Applications (2012)

[48] Tracy, M.B.: Cavity unsteady-pressure measurements at subsonic and transonic speeds. NASA, Langley Research Center **3669** (1997)

[49] Yokoyama, H., Odawara, H., Iida, A.: Effects of freestream turbulence on cavity tone and sound source. International Journal of Aerospace Engineering **2016** (2016)